Journal of Luminescence 170 (2016) 627–632

Contents lists available at ScienceDirect

Journal of Luminescence

journal homepage: www.elsevier.com/locate/jlumin

Valence control of Pr in ZrO_2 nanocrystals by aliovalent Gd^{3+} co-doping

José M. Carvalho [a,b], Mika Lastusaari [b,c], Lucas C.V. Rodrigues [a], Jorma Hölsä [a,b,c], Maria C.F.C. Felinto [d], Hermi F. Brito [a]

[a] University of São Paulo, Institute of Chemistry, São Paulo, SP, Brazil
[b] University of Turku, Department of Chemistry, Turku, FI 20014, Finland
[c] Turku University Centre for Materials and Surfaces (MatSurf), Turku, Finland
[d] Institute of Energy and Nuclear Research, São Paulo, SP, Brazil

ARTICLE INFO

Article history:
Received 31 January 2015
Received in revised form
9 June 2015
Accepted 9 July 2015
Available online 17 July 2015

Keywords:
Praseodymium luminescence
Valence control
Cross-relaxation
Nanocrystals

ABSTRACT

Praseodymium doped ZrO_2 materials were prepared *via* sol–gel route and structurally characterized by X ray powder diffraction (XPD) technique as well as *Rietveld* refinements. The addition of the Gd^{3+} co-dopant gradually changes the zirconia structure from monoclinic to tetragonal, and then to cubic. Intensification of the Pr^{3+} luminescence was observed with the increasing Gd^{3+} co-dopant concentration. Emission spectra of the $Zr_{0.99-x}Gd_xPr_{0.01}O_2$ materials show an initial strengthening of the red emission of Pr^{3+} ($^1D_2 \rightarrow {}^3H_4$ transition) with increasing Gd^{3+} co-doping. However, the luminescence is quenched at the highest Gd^{3+} concentration-possibly due to strongly increased concentration of the charge compensation defects. The valence change ($Pr^{IV} \rightarrow Pr^{3+}$) is supported by the XANES results on the L_{III} edge of Pr. Although predominantly in the Pr^{3+} form irrespective of the Gd^{3+} concentration, the contribution from Pr^{IV} is clearly visible at low (or zero) Gd^{3+} concentrations leading to the loss of Pr^{3+} and to poor luminescence output. Though enhancing the emission intensity of Pr^{3+}, the defect clusters engender short Pr^{3+}–Pr^{3+} distances enhancing the cross-relaxation process coupling the $^3P_0 \rightarrow {}^1D_2$ relaxation with the $^3H_4 \rightarrow {}^3H_6$ excitation. This process leads to the high red/blue–green emission ratio by quenching the $^3P_0 \rightarrow {}^3H_4$ transition in blue–green. Eventually, the increased Gd^{3+} co-doping dilutes the Pr^{3+} ions and, the cross-relaxation process becomes non-operational; the quenching of the $^3P_0 \rightarrow {}^3H_4$ transition is reversed.

1. Introduction

The different rare earth (R^{n+}) valences can affect largely the optical properties of the materials and consequently the further applications [1–4]. In some cases it can quench dramatically the luminescence by recombination processes or energy transfer [1,5]. Accordingly, different processes in luminescent material preparation such as heating in a reducing atmosphere [6], carbothermal reduction [7] and pulsed-laser deposition [8] are developed to control the valence of the R^{n+} ions and obtain selected optical properties. For example, to obtain the $SrAl_2O_4$:Eu^{2+},Dy^{3+} persistent luminescence material with Eu^{2+} a reducing atmosphere furnace [6,9] is used, also sol–gel [10] and combustion [11,12] synthesis can be used to improve the reduction of Eu^{3+} ion. Several studies about the valence state of Eu in different materials can be found in literature [13–15], due to the importance of this activator in a variety of phosphors. On the other hand, studies on the valence control of other rare earth with multi-oxidation states, such as $Pr^{3+/IV}$ and $Tb^{3+/IV}$, can be found in a less extension [16–18]. Phosphors containing Pr ions must have preferentially the trivalent state, because the tetravalent form can act as luminescence quencher.

The valence state of R ions may depend on its reduction potential, the chemical environment and defect structure of a particular material. However, the present models of the valence control of rare earths in materials seems inconclusive [19]. The effect of the rare earth environment and different defects in the materials (like oxygen vacancies) or even size effects of relative position of the dopants can drastically change or tune their valences [13,14].

Despite the large number of reports on rare earth doped zirconia [20–27], the knowledge about the valence change of key R doped zirconia is still serendipitously poor. For many applications, the ZrO_2 materials are stabilized with yttria generating the yttria-

E-mail address: hefbrito@iq.usp.br (H. F. Brito).

http://dx.doi.org/10.1016/j.jlumin.2015.07.009
0022-2313/

stabilized-zirconia (YSZ) [28]. The luminescence properties of the Tb and Pr doped YSZ has thus been reported frequently [29,30]. The enhancement of red luminescence in the Pr^{3+} doped YSZ was attributed to sensitization by the Y^{3+} co-doping [17]. Recently, the reduction of Tb^{IV} to Tb^{3+} in ZrO_2 host was reported by our group [18], as an effect of Yb^{3+} aliovalent co-doping, causing an increase of the luminescence efficiency.

In this work, ZrO_2:Pr,Gd^{3+} nanomaterials were synthesized using a simple one-step sol–gel method and the red luminescence intensity of Pr^{3+} was correlated with the valence of the ions which can be modulated changing the defect structure of the materials. The influence of the crystalline structure on the luminescence process was discussed as well.

2. Experimental

2.1. Material and synthesis

The ZrO_2:Pr,Gd^{3+} nanomaterials were prepared by a conventional sol–gel method [31,32], where the zirconium tetrabutoxide (ZTB, 70 wt%, 1-butanol solution, Sigma-Aldrich) was hydrolyzed with a controlled amount of water dissolved in isopropanol for the molar ratio $W=[H_2O]/[ZTB]=3$. In a typical synthesis, 4 cm^3 of ZTB was added in a round bottomed flask containing 25 cm^3 of dry 1-butanol. The homogeneous solution was capped and stirred for 15 min and then the water/*i*PrOH solution was added dropwise. The $R(NO_3)_3$•$6H_2O$ salts (R: Pr and Gd) were obtained by dissolving Pr_6O_{11} and Gd_2O_3 (99.99%, C-STARM) in HNO_3 (70% v/v, Vetec) and then added in the water/*i*PrOH solution to obtain the doped materials. The formed gel-like dispersion was allowed to react for 24 h at room temperature (298 K) without stirring. In the next step, the crude gel was dried at 110 °C for 12 h. The dried gel was ground in a mortar and finely divided powders were obtained. The as-prepared materials were further annealed at 1000 °C for 5 h, yielding $Zr_{0.99-x}Gd_xPr_{0.01}O_2$ (x_{Gd}: 0.01, 0.05, 0.10 and 0.20) nanocrystals.

2.2. Characterization

The crystal structure of the materials was verified with the X-ray powder diffraction measurements using a Huber G670 diffractometer with $CuK_{\alpha1}$ (1.5405 Å) radiation between 15 and 70 degrees (in 2θ) with 0.005 degree 2θ step and 60 min data collection.

Rietveld refinements were carried out using the general structure analysis system (GSAS) and illustrated by VESTA software.

The transmission electron microscopy imaging (TEM) of the Pr–Gd ZrO_2 co-doped materials were carried out with a JEOL JEM 2100F from the Laboratório Nacional de Luz Síncrotron (LNLS, Campinas, Brazil).

The photoluminescence measurements on the zirconia materials were carried out at room temperature with a SPEX Fluorolog-2 spectrofluorimeter equipped with two 0.22 m SPEX 1680 double grating monochromators. A 450 W Xenon lamp was used as the excitation source. The excitation and emission spectra were collected at an angle of 22.5 degrees (front face). All spectra were recorded using automatic detector mode correction. The near-infrared spectra for the zirconia materials were carried out at room temperature with a FieldSpec HandHeld Pro Spectroradiometer.

The valence and environment of Pr and Gd in ZrO_2 were studied by XANES and EXAFS measurements at 10 K. Beamline A1 at the Hamburger Synchrotronstrahlungslabor (HASYLAB) at Deutsches Elektronen–Synchrotron (DESY) (Hamburg, Germany) was used. Data was collected on the Pr L_{III} and Gd L_{III} edges using a Si (111) double crystal monochromator. The measurements were carried out in fluorescence mode using a SDD-MI 7 channel silicon drift detector.

3. Results and discussion

3.1. Structural analysis

The ZrO_2 matrix has three different polymorphs: monoclinic (space group: $P2_1/c$), tetragonal ($P4_2/nmc$) and cubic ($Fm\bar{3}m$). Monoclinic zirconia has a seven coordinated Zr site with a distorted monocapped octahedral coordination polyhedron whereas the tetragonal and cubic phases have eight coordinated sites with cubic-like coordination polyhedron. The monoclinic phase is the stable phase at room temperature and pressure. Nevertheless, it is possible to obtain the tetragonal and cubic phases at room temperature using trivalent (*e.g.* Y^{3+}) or even divalent (*e.g.* Ca^{2+}) dopants to create the so-called stabilized zirconia. The stabilization occurs due to the aliovalent substitution of Zr^{IV}, which can create a proximal structural defects, mostly oxide vacancies ($\ddot{V}_o$). The usual representation to the structural defects is the Kroger–Vink notation [33].

XRD patterns (Fig. 1) of the zirconia nanomaterials with increasing dopant concentrations confirm the monoclinic (*m*-ZrO_2), tetragonal (*t*-ZrO_2) and cubic (*c*-ZrO_2) structures as a co-dopant stabilization effect [31,32,34]. For low dopant concentration, the material crystallizes as *m*-ZrO_2 that is the thermodynamically stable phase of non-doped ZrO_2 at 298 K. When the trivalent dopant (R^{3+}: Pr or Gd) substitution in the Zr^{IV} sites increases, the number of oxygen vacancies created by charge compensation (R'_{zr}–$\ddot{V}_o$–R'_{zr}) displaces the oxygen positions, allowing the structural stabilization [35], first to tetragonal phase and then to cubic at higher Gd^{3+} concentrations [36]. The Rietveld refinements converged to good fits, yielding good values of χ^2 in the range of 2–3 for the data set.

The cell parameters (Table 1) obtained from the Rietveld refinement show an expected expansion of the lattice, due to the

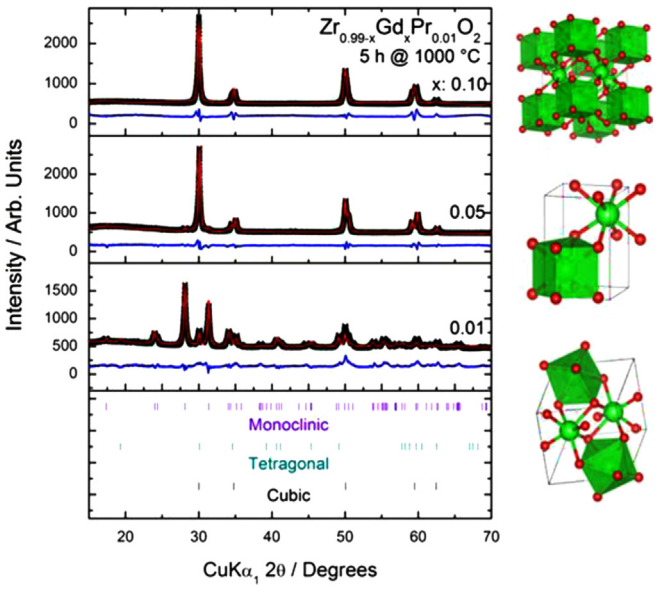

Fig. 1. The XPD data including the Rietveld refinements for $Zr_{0.99-x}Gd_xPr_{0.01}O_2$. The symbols, solid lines and bars represent experimental data, calculated and difference plots and Bragg's reflection positions, respectively. The structures derived from refinements are the monoclinic (bottom), tetragonal (middle) and cubic (top) ZrO_2.

incorporation of the larger R^{3+} ion [r_{eff}: 1.126 (Pr^{3+}) and 1.053 Å (Gd^{3+}); $CN=8$] replacing the smaller Zr^{IV} ($r_{eff}=0.84$ Å; $CN=8$) [37]. The tetragonal and cubic zirconia phases have smaller cell volume compared to the monoclinic one, partly due to the higher concentration of oxygen vacancies allowing a degree of contraction for the Zr–O bonds. This effect can be seen in the lattice parameters for the cubic structure, which has smaller *a* cell parameter, even containing higher dopant concentration.

The formation of oxygen vacancies because of charge compensation seems to cancel partially the unit cell expansion. No segregation of cubic R_2O_3 was observed in materials. The structures based on the Rietveld refinements (Fig. 1, right) indicate decreasing structural distortions from monoclinic to cubic phase, as shown by the distortion index parameters (Table 1). This result suggests that the co-dopant is not disturbing considerably the average crystal structure.

Table 1
Refined structural cell parameters, phase proportion and distortion index related to the bond length of the zirconium coordination polyhedral on major refined phase.

$Zr_{0.99-x}Gd_xPr_{0.01}O_2$		*a*	*b*	*c*	Distortion index (bond length)
x_{Gd}:0.01	Monoclinic (83.2%)	5.1644(5)	5.2175(7)	5.3294(6)	0.064
	Tetragonal (16.8%)	3.6065(5)	$a=b$	5.1865(7)	
x_{Gd}:0.05	Monoclinic (2.2%)	5.1206(4)	5.2270(4)	5.3450(4)	0.023
	Tetragonal (97.8%)	3.6123(6)	$a=b$	5.1872(2)	
x_{Gd}:0.10	Cubic (100%)	5.1457(9)			0.000

3.2. Particle morphology

Two main chemical reactions govern the sol–gel process: hydrolysis and condensation. Many parameters can affect the hydrolysis rate [38–40], such as solvent polarity, water concentration in the synthesis, ionic strength, etc. The addition of crescent concentrations of hydrated rare earth nitrates in the precursor solution makes the hydrolysis rate increases, forming bigger agglomerates. The transmission electron microscopy (TEM) was used to investigate the particle size of the materials and aggregation was observed as a function of dopant concentration (Fig. 2). The nanocrystals synthesized with x_{Gd}:0.01 have very good dispersion with size distribution at around 50 nm. The formation of the nanocrystals by sol–gel method is very dependent of the concentration of rare earth salt precursors, yielding different agglomeration, but relatively similar particle sizes. For higher concentrations of Gd^{3+} co-dopant the agglomeration is more evident, however the material is still composed by ZrO_2 nanocrystals with 40–50 nm. The using of a stabilizing agent may be useful to obtain more disperse luminescent nanoparticles.

Despite the fact of the agglomeration, it is still possible to observe some square flat faces for the 5 and 10% Gd^{3+} co-doping, which is attributed to tetragonal and cubic zirconia nanocrystals stabilized by the R^{3+} ions. The existence of nanocrystals with less than 40 nm of m-ZrO_2 indicates that metastable tetragonal phase

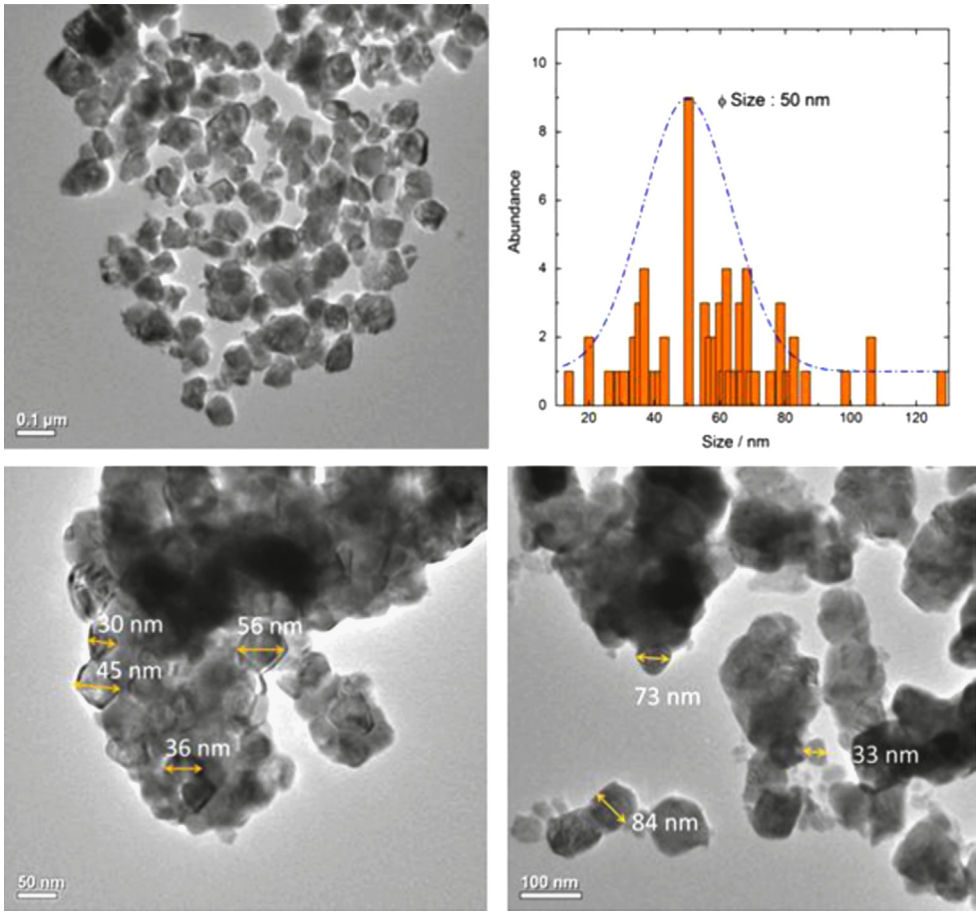

Fig. 2. Transmission electron images of the $Zr_{0.99-x}Gd_xPr_{0.01}O_2$ for x_{Gd}:0.01 (top left), 0.05 (bottom left) and 0.10 (bottom right). The size distribution (top right) is related to image with x_{Gd}:0.01.

is not observed as "precursor" of monoclinic in zirconia sol–gel materials [41].

3.3. Valence state and chemical environment of Pr ion

X ray absorption near edge structure (XANES) spectroscopy was used to study the valence state of the praseodymium ion doped in the $Zr_{0.99-x}Gd_xPr_{0.01}O_2$ materials (Fig. 3). The XANES spectrum of Pr_6O_{11} compound shows two maxima around the absorption edge. The higher energy (5981 eV) corresponds to the final state $\underline{2p}^4f^15d^*$ (_denotes a hole and * an excited electron) for Pr^{IV} ion. The lower energy maximum (5969 eV) is due to Pr^{3+} ($\underline{2p}^4f^25d^*$) and Pr^{IV} by the occupation of localized 4f orbitals in the core-excited final state *via* 4f-ligand (L) covalency ($\underline{2p}^4f^25d^*\underline{L}$). The latter contribution is also observed for Ce^{IV} and Tb^{IV} reported in reference [42]. Therefore, the ratio of the integrated areas of the two peaks does not give directly the valence of Ce, Pr or Tb, but it still gives a qualitative indication of the valence states of each cation. The Pr L_{III} edge XANES spectra of the ZrO_2:Pr,Gd materials show that Pr^{IV} is clearly present with x_{Gd}: 0.00, 0.01 and 0.05 concentrations. The presence of some Pr^{IV} in the material with x_{Gd}:

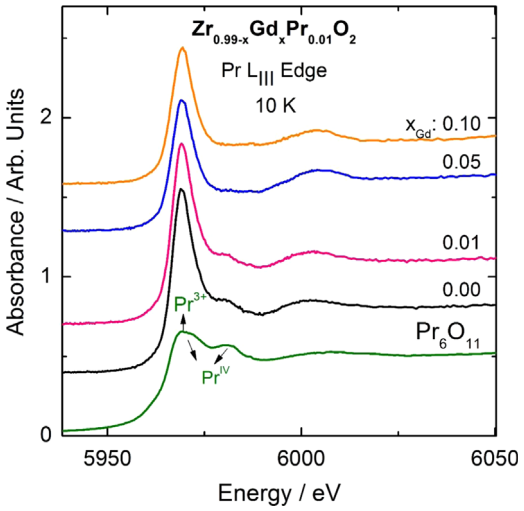

Fig. 3. Synchrotron X ray near edge structure (XANES) spectra for the set of materials centered on the Pr (L_{III}) edge at 10 K. The Pr_6O_{11} spectrum is is presented as reference.

0.10 cannot be completely ruled out because the of the Gd L_{III} XANES spectral feature (figure not shown) show a small drop instead of an almost vertical signal after the white line. Thus, the Gd^{3+} concentration is responsible to the valence change of Pr ion ($Pr^{IV} \rightarrow Pr^{3+}$). The same effect of valence control was observed in a previous work for Tb–Yb co-doped zirconia, where the Yb concentration affects the Tb valence [18].

In synthesis of ZrO_2:Pr,Gd materials, trivalent praseodymium nitrate was used as precursor and tends to oxidate to Pr^{IV} after thermal treatment. When the concentration of the Gd co-dopant increases, the number of defect clusters (R'_{zr}–$\ddot{V}_o$–R'_{zr}) increases, involving also Pr^{3+} ion, which stabilize the trivalent state ($Pr^{IV} \rightarrow Pr^{3+}$). The created oxide vacancies could store the electrons liberated in the redox process $Pr^{3+/IV}$ pair forming a dynamic Pr^{3+}/Pr^{IV} couple with concentration ratio depending on the available external energy (mostly *k*T). Other studies are needed to check the energy level position of aliovalent dopants in the bandgap and correlate with the Fermi level of the material.

The calculated distance distributions around Gd^{3+} ion are rather similar with all Gd concentrations (Fig. 4). The Gd–O distances indicate that with x_{Gd}:0.05 and 0.10, the structure is close to cubic, but monoclinic cannot be completely ruled out (Fig. 4). With x_{Gd}:0.01, monoclinic seems more dominant. The Gd–O distances are always longer than the Zr–O ones, as expected from the differences of the respective ionic radii, *i.e.* r_{eff}: (Gd^{3+}: 1.05, CN: 8) and r_{eff}: (Zr^{IV}: 0.84 Å, CN: 8) [37].

The distance distributions around Pr are not completely similar to those around Gd. For the materials without gadolinium (x_{Gd}:0.0) the Pr–O distance (*ca.* 2.5 Å) is clearly more than expected, which is since the ionic radius of Pr^{3+} (1.13 Å [37]) is not far from that of Gd^{3+}. Moreover, the presence of Pr^{IV} (0.96 Å [37]) should decrease Pr–O distance. As the EXAFS calculations indicate that the Pr–O distances are shorter than the Gd–O ones, except to the x_{Gd}:0.0 one, the results support the presence of Pr^{IV}. Based on EXAFS calculations, the distances around Pr suggest monoclinic, cubic and tetragonal (local) structures for x_{Gd}: 0.01, 0.05 and 0.10, respectively.

3.4. Photoluminescence study of the ZrO_2:Pr^{3+} nanocrystals

The emission spectra of $Zr_{0.99-x}Gd_xPr_{0.01}O_2$ (x_{Gd}:0.01, 0.05, 0.10 and 0.20) nanocrystals (Fig. 5, left) are composed of narrow emission bands assigned to 4f–4f transitions of Pr^{3+}, with most intense transition peaking at *ca.* 620 nm. All materials show

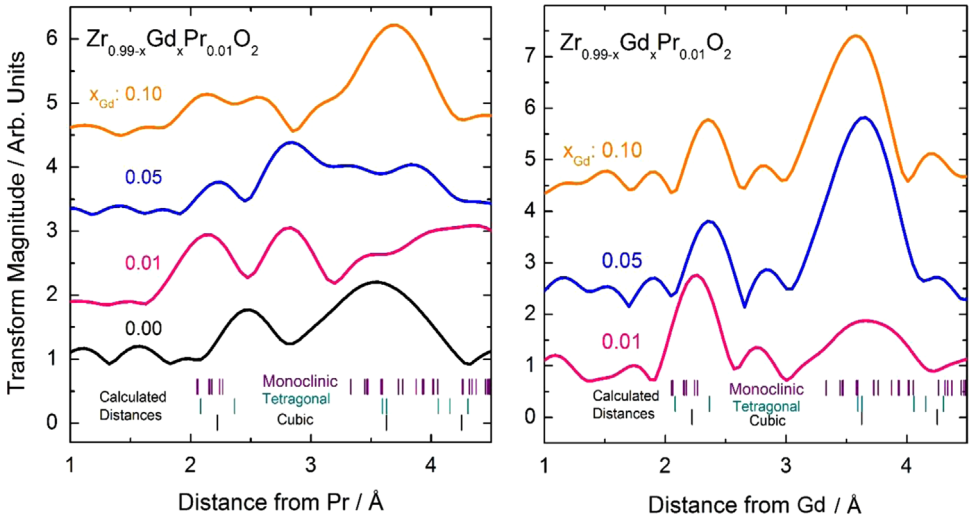

Fig. 4. Distance distributions calculated from the Synchrotron radiation EXAFS spectra for the set of materials centered on the Pr (L_{III}) (left) and Gd (L_{III}) edge. The measurements were conducted at 10 K.

orange–red emission color under UV excitation (~300 nm) due to Pr^{3+} 4f-5d absorption band. The excitation on the visible range (*ca.* 450 nm) is also possible due to the Pr^{3+} energy level structure; however, the resultant emission is less intense. The site symmetry for the praseodymium site is changing from low to higher symmetry (C_{2h} to O_h) with the increase of the Gd^{3+} concentration.

However, no considerable difference is observed in the emission band splitting of 4f transitions of the Pr^{3+} ion, probably due to the nanoparticle size effect. Integrated intensity bands of the $^1D_2 \rightarrow {}^3H_4$ (red) and $^3P_0 \rightarrow {}^3H_4$ (green) transitions of the $Zr_{0.99-x}Gd_xPr_{0.01}O_2$ materials (Fig. 5, right) show an enhancement of the red emission intensity of Pr^{3+} (mainly the $^1D_2 \rightarrow {}^3H_4$ transition) with increasing Gd^{3+} co-doping from 0.01 to 0.10. However, it is observed the luminescence quenches at the highest Gd^{3+} concentration (0.20), possibly due to charge compensation defects. The emission intensity changing of Pr^{3+} as a function of Y^{3+} co-doping was investigated in literature [17], showing an increase in the luminescence output with increasing Y^{3+} content, which was attributed to Y^{3+} sensitization of the Pr^{3+}. However, the enhancement of the red emission intensity is due to the conversion of Pr^{IV} to Pr^{3+} causing an increasing of the Pr^{3+} concentration, as showed unambiguously by the XANES spectra (Fig. 3).

The higher contribution of the red emission of Pr^{3+} ion indicates that a cross-relaxation path for the blue–green emission must be operative. This is an evidence for the short Pr^{3+}–Pr^{3+} distances promoted by praseodymium clustering. Cross-relaxation processes between two Pr^{3+} ions (Fig. 6, right) is a distance dependent phenomenon, coupling the $^3P_0 \rightarrow {}^1D_2$ relaxation with the $^3H_4 \rightarrow {}^3H_6$ excitation of Pr^{3+} ion. With the increasing of Gd^{3+} concentration (from x_{Gd}: 0.01–0.20) the clustering probability changes, and then more cluster of Pr^{3+}–Gd^{3+} are possible. At lower concentrations of Gd^{3+} (x:0.01) it is possible to observe very weak emission coming from Pr^{3+} ions (Fig. 5, left – insert figure).

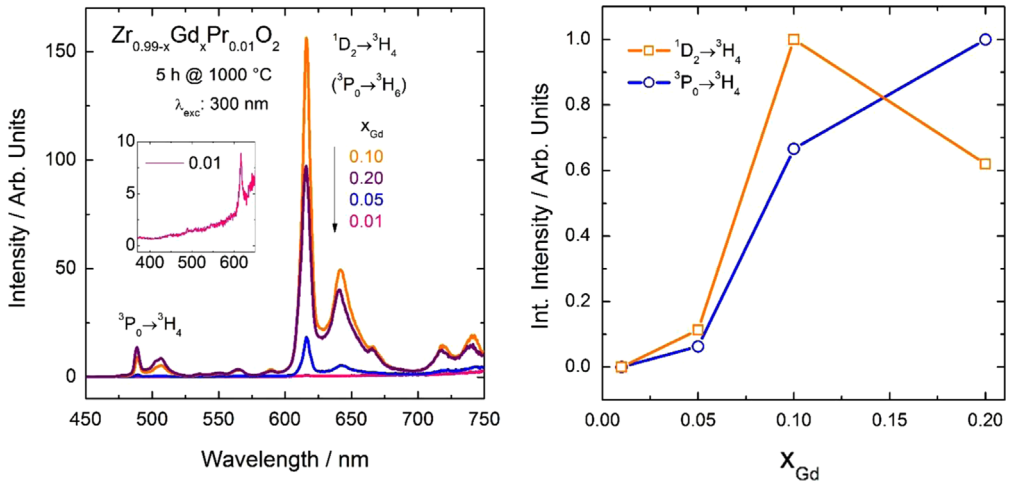

Fig. 5. Emission spectra for the $Zr_{0.99-x}Gd_xPr_{0.01}O_2$ nanocrystals, obtained by sol–gel method (left). Integrated intensity for the $^1D_2 \rightarrow {}^3H_4$ (orange) and $^3P_0 \rightarrow {}^3H_4$ (blue) transitions of Pr^{3+} ion (right). The excitation was centered in 300 nm and all experiments were carried out at room temperature. (For interpretation of the references to color in this figure legend, the reader is referred to the web version of this article.)

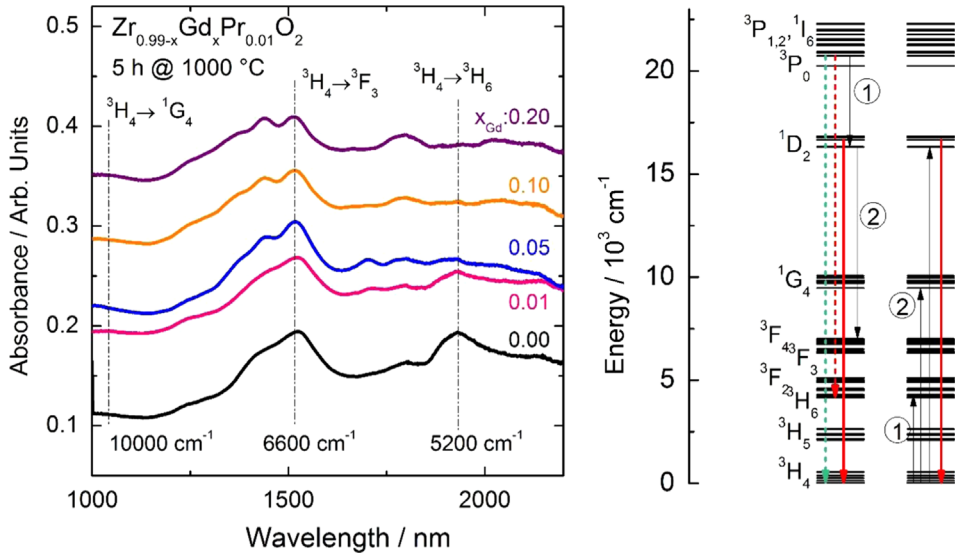

Fig. 6. Near-Infrared absorption spectra for the set of materials showing the low energy infrared transitions of Pr^{3+} ion (left). Praseodymium energy level diagram showing the mechanism of cross-relaxation path for blue–green transition hindering (right). (For interpretation of the references to color in this figure legend, the reader is referred to the web version of this article.)

The monoclinic phase of $Zr_{0.99-x}Gd_xPr_{0.01}O_2$ materials present the weakest emission intensity arising from the Pr^{3+} in comparison with tetragonal and cubic and similar photoluminescent behavior was also observed to the Tb doped ZrO_2 reported in reference [18]. Besides, the $CdSiO_3$ matrix doped with Pr and Tb ions show the luminescence from the rare earth ions, which are very dependent to the bandgap of the material [43].

The $^3H_4 \rightarrow {}^3H_6$ transitions of Pr^{3+} ion present in the near-infrared absorption spectra of the $Zr_{0.99-x}Gd_xPr_{0.01}O_2$ materials become less intense with increasing Gd^{3+} concentration (Fig. 6, left), due to monoclinic to tetragonal/cubic phase transition. The different structures lead to different oscillator strengths, and different green/red emission ratio, consequently.

4. Conclusions

High quality nanocrystals of $Zr_{0.99-x}Gd_xPr_{0.01}O_2$ materials were successfully prepared using a one-step sol–gel method and structurally characterized by XPD techniques along with Rietveld refinement. The elongated cell parameters for all three phases indicate that Pr and Gd ions substitute the Zr site in the structure. The formation of oxygen vacancies partially cancels the unit cell expansion due to charge compensation. The TEM images showed nanocrystals with 40–50 nm size range for all set of materials, however, the agglomeration of the particles increase with the increasing dopant concentration. Monoclinic nanocrystal with less than 40 nm indicates that metastable tetragonal zirconia is not the precursor of the monoclinic phase in the materials. Red emission color arising from all materials is assigned mainly to the $^1D_2 \rightarrow {}^3H_4$ transition of Pr^{3+} ion. The emission intensity of the Pr^{3+} is increased with the Gd^{3+} content due to redox conversion of Pr^{IV} to Pr^{3+} assisted by defect clusters formation. The luminescence quenching is observed at higher Gd^{3+} doping concentration, due to increased concentration of defect clusters. Enhancement of the cross-relaxation process coupling the $^3P_0 \rightarrow {}^1D_2$ relaxation with the $^3H_4 \rightarrow {}^3H_6$ excitation was observed. The absorption band assigned to $^3H_4 \rightarrow {}^3H_6$ transition becomes less intense with the increasing of Gd^{3+} content hindering the cross-relaxation process and increasing the blue–green emission. The valence control of Pr^{3+} in ZrO_2 materials is an important issue, since no luminescent efficient Pr or Tb doped ZrO_2 materials have been prepared so far, due to inherent oxidation of these rare earths when substituted into the Zr^{IV} lattice. This study can open an avenue to prepare luminescence materials with desired optical properties controlling only the synthesis parameters.

Acknowledgments

Financial support is gratefully acknowledged from the Conselho Nacional de Desenvolvimento Científico e Tecnológico (CNPq) (Grant Number 490435/2009-2 and 490242/2012-0) and the Academy of Finland through the Brazil-Finland Bilateral Project in the Photonics program, the Coordenação de Aperfeiçoamento de Pessoal de Nível Superior (CAPES) (078/2009/DBP), the Fundação de Amparo à Pesquisa do Estado de São Paulo (FAPESP), and the Instituto Nacional de Ciência e Tecnologia-Nanotecnologia para Marcadores Integrados (inct-INAMI) (Grant number: 5739862-2008-8). The authors thank the Laboratório Nacional de Luz Síncrotron (LNLS-Campinas) and LNNANO for the usage of the transmission electron microscopy facilities.

References

[1] M. Kitsuda, S. Fujihara, J. Phys. Chem. C 115 (2011) 8808.
[2] M. Peng, Z. Pei, G. Hong, Q. Su, J. Mater. Chem. 13 (2003) 1202.
[3] M. Peng, Z. Pei, G. Hong, Q. Su, Chem. Phys. Lett. 371 (2003) 1.
[4] S. Kunimi, S. Fujihara, J. Solid State Sci. Technol. 1 (2012) R32.
[5] Y.H. Wang, J.C. Zhang, X. Guo, Electrochem. Solid-State Lett. 9 (2006) H26.
[6] J. Qiu, K. Hirao, Solid State Commun. 106 (1998) 795.
[7] X. Piao, T. Horikawa, H. Hanzawa, K. Machida, Chem. Lett. 35 (2006) 334.
[8] A. Pillonnet, A. Pereira, O. Marty, C. Champeaux, J. Phys. D: Appl. Phys. 44 (2011) 375402.
[9] T. Matsuzawa, Y. Aoki, N. Takeuchi, Y. Murayama, J. Electrochem. Soc. 143 (1996) 2670.
[10] T. Peng, L. Huajun, H. Yang, C. Yan, Mater. Chem. Phys. 85 (2004) 68.
[11] T. Peng, H. Yang, X. Pu, B. Hu, Z. Jiang, C. Yan, Mater. Lett. 58 (2004) 352.
[12] L.C.V. Rodrigues, J. Hölsä, J.M. Carvalho, C.C.S. Pedroso, M. Lastusaari, M.C.F. C. Felinto, et al., Phys. B: Condens. Matter 439 (2014) 67.
[13] K. Huang, W. Chen, C. Chu, S. Hu, H. Sheu, B. Cheng, et al., Chem. Mater. 24 (2012) 2220.
[14] N. Avci, K. Korthout, M.A. Newton, P.F. Smet, D. Poelman, Opt. Mater. Express 2 (2012) 321.
[15] A. Nag, T.R.N. Kutty, J. Mater. Chem. 14 (2004) 1598.
[16] M. Zhuravleva, S. Friedrich, C.L. Melcher, Appl. Phys. Lett. 101 (2012) 101902.
[17] J.D. Fidelus, S. Yatsunenko, M. Godlewski, W. Paszkowicz, Scr. Mater. 61 (2009) 415.
[18] I.A.A. Terra, L.J. Borrero-González, J.M. Carvalho, M.C. Terrile, M.C.F.C. Felinto, H.F. Brito, et al., J. Appl. Phys. 113 (2013) 073105, http://dx.doi.org/10.1063/1.4792743.
[19] M. Ping, G. Hong, J. Lumin. 127 (2007) 735.
[20] M. Zelner, A. Patra, J. Alloy. Compd. 301 (2000) 147.
[21] K. Smits, L. Grigorjeva, D. Millers, A. Sarakovskis, A. Opalinska, J.D. Fidelus, et al., Opt. Mater. (Amst) 32 (2010) 827.
[22] R. Reisfeld, M. Zelner, A. Patra, J. Alloy. Compd. 300–301 (2000) 147.
[23] A. Mondal, A. Zachariah, P. Nayak, B.B. Nayak, J. Am. Ceram. Soc. 93 (2010) 387.
[24] T.K. Anh, L. Quoc Minh, N. Vu, T. Thu Huong, N. Thanh Huong, C. Barthou, et al., J. Lumin. 102–103 (2003) 391.
[25] X. Fu, S. Niu, H. Zhang, Q. Xin, Mater. Sci. Eng. B 129 (2006) 14.
[26] H. Yahiro, Solid State Ion. 36 (1989) 71.
[27] E. De la Rosa-Cruz, L.A. Díaz-Torres, P. Salas, D. Mendoza, J. Hernández, V. Castaño, Opt. Mater. (Amst). 19 (2002) 195, http://dx.doi.org/10.1016/S0925-3467(01)00219-1.
[28] Y. Liu, J. Kuang, B. Lei, C. Shi, J. Mater. Chem. 15 (2005) 4025.
[29] M.R.N. Soares, C. Nico, J. Rodrigues, M. Peres, M.J. Soares, A.J.S. Fernandes, et al., Mater. Lett. 65 (2011) 1979.
[30] P.K. Wright, A.G. Evans, Curr. Opin. Solid State Mater. Sci. 4 (1999) 255.
[31] L.L. Hench, J.K. West, Chem. Rev. 90 (1990) 33.
[32] J.M. Carvalho, L.C.V. Rodrigues, M.C.F.C. Felinto, L.A.O. Nunes, J. Hölsä, H. F. Brito, J. Mater. Sci. (2014).
[33] F.A. Kröger, H.J. Vink, J. Phys. Chem. Solids 5 (1958) 208.
[34] J.M. Carvalho, L.C.V. Rodrigues, J. Hölsä, M. Lastusaari, L.A.O. Nunes, M.C.F. C. Felinto, et al., Opt. Mater. Express 2 (2012) 331.
[35] M. Yashima, M. Kakihana, M. Yoshimura, Solid State Ion. 86–88 (1996) 1131.
[36] M.R.N. Soares, M.J. Soares, A.J.S. Fernandes, L. Rino, F.M. Costa, T. Monteiro, J. Mater. Chem. 21 (2011) 15262.
[37] R.D. Shannon, Acta Crystallogr. A32 (1976) 751.
[38] R.E. Hann, P.R. Suitch, J.L. Pentecost, J. Am. Ceram. Soc. 68 (1985) 285.
[39] H. Boysen, F. Frey, T. Vogt, Acta Crystallogr. Sect. B 47 (1991) 881.
[40] J. Jaffe, R. Bachorz, M. Gutowski, Phys. Rev. B. 72 (2005) 144107.
[41] C. Garvie, J. Phys. Chem. 69 (1965) 1238.
[42] L.Z. Linganiso, G. Jacobs, K.G. Azzam, U.M. Graham, B.H. Davis, D.C. Cronauer, et al., Appl. Catal. A Gen. 394 (2011) 105.
[43] L.C.V. Rodrigues, M. Lastusaari, H.F. Brito, M.C.F.C. Felinto, J.M. Carvalho, J. Hölsä, et al., Phys. Scr. 89 (2014) 044014.